Science Advances
AAAS

advances.sciencemag.org/cgi/content/full/5/10/eaax9501/DC1

# Supplementary Materials for

## Stimulated transformation of soft helix among helicoidal, heliconical, and their inverse helices

Cong-long Yuan, Wenbin Huang, Zhi-gang Zheng*, Binghui Liu, Hari Krishna Bisoyi, Yannian Li, Dong Shen, Yanqing Lu*, Quan Li*

*Corresponding author. Email: zgzheng@ecust.edu.cn (Z.-g.Z.); yqlu@nju.edu.cn (Y.Lu); qli1@kent.edu (Q.L.)

Published 4 October 2019, *Sci. Adv.* **5**, eaax9501 (2019)
DOI: 10.1126/sciadv.aax9501

**This PDF file includes:**

# S1. Theoretical background of the heliconical superstructure formation

Cholesteric liquid crystal (CLC) material with a very small bend elastic constant $K_3$ under delicate competition between dielectric torque and chirality, is capable of forming the heliconical superstructure, also known as the oblique helicoidal structure (*33*,*34*). In the heliconical superstructure, the liquid crystal (LC) director twists around the helical axis and makes an oblique angle with this direction. The electric-field applied parallel to the helical axis can change the pitch and the oblique angle without rotating the helical axis. In this section, we demonstrate the theoretical framework of the cholesteric heliconical superstructure with the presence of the electric-field.

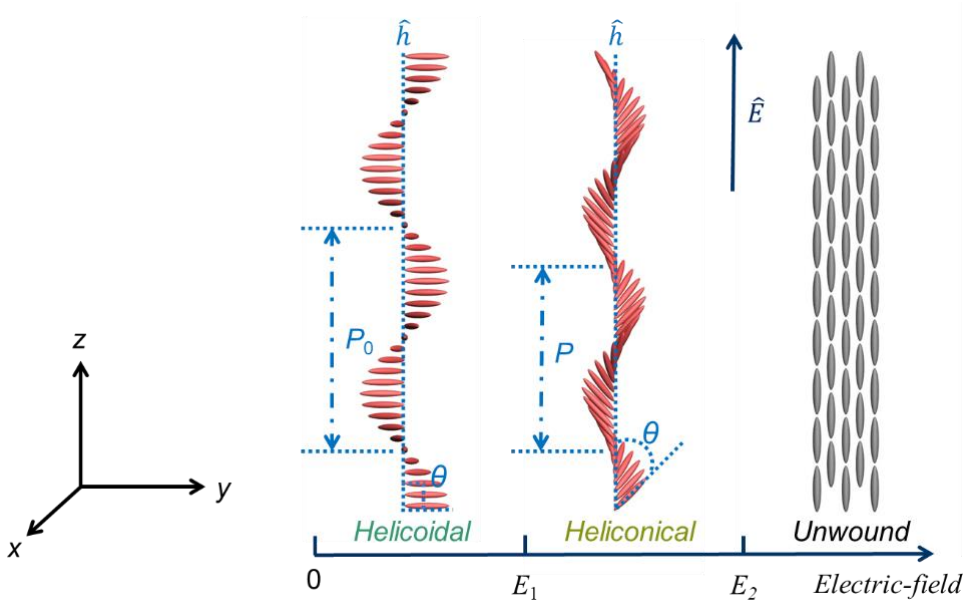


**Fig. S1. Schematic illustration of LC director configurations in helicoidal, heliconical, and unwound superstructures as a function of the electric field.**

The electric-field induced LC director arrangement can be described by using the Oseen-Frank free energy function. The energy density for CLC can be written as

$$f = \frac{1}{2}\left[ K_1 \left(\nabla \cdot \hat{n}\right)^2 + K_2 \left(\hat{n} \cdot \nabla \times \hat{n} - q_0\right)^2 + K_3 \left(\hat{n} \times \nabla \times \hat{n}\right)^2 - \Delta\varepsilon\varepsilon_0 \left(\hat{n} \cdot \vec{E}\right)^2 \right] \quad \text{(S1)}$$

where $K_1$, $K_2$ and $K_3$ are the splay, twist, and bend elastic constant, respectively; ***n*** is a unit vector denoting the LC director; $q_0=2\pi/P_0$, representing the chirality; $P_0$ is the initial pitch length of CLC system; $\Delta\varepsilon$ is the dielectric anisotropy standing for

the difference between the dielectric constant along the long axis and that along the short axis of the LC director; $\varepsilon_0$ is the permittivity of vacuum; ***E*** is the applied electric-field. Here, we consider a longitudinal electric-field is parallel to the helical axis ***h*** (*z* axis) which can be written as

$$\vec{E} = \left(0, \quad 0, \quad E\right) \tag{S2}$$

Since the CLC system have a positive dielectric anisotropy ($\Delta\varepsilon$ >0), LC director will tend to orient along the electric-field.

By minimizing the free energy, we can obtain the following three types of stacking configurations of LC molecules as indicated in fig. S1. Without the external electric-field, chirality guides the LC molecules to self-organize into the helicoidal superstructure (also named right-angle helicoid), in which the LC director twists around the helical axis ***h*** with a right-angle. Then the director ***n*** is given by

$$n = \left(\cos\left(\frac{2\pi}{P_0}z\right), \quad \sin\left(\frac{2\pi}{P_0}z\right), \quad 0\right) \tag{S3}$$

For an electric-field between a lower induction threshold value $E_1$ and an upper unwinding threshold value $E_2$, the dielectric torque can compete with the twist toque, forming the heliconical superstructure (also called oblique helicoid) where the director spirals around the helical axis ***h*** with an oblique angle $\theta$ ($0<\theta<\pi/2$). Then the director ***n*** in heliconical state can be written as

$$n = \left(\cos\left(\frac{2\pi}{P}z\right)\sin\theta, \quad \sin\left(\frac{2\pi}{P}z\right)\sin\theta, \quad \cos\theta\right) \tag{S4}$$

Further increasing the electric-field beyond the threshold value $E_2$ unwinds the helix state into the homeotropic alignment of LC molecules. Then the director ***n*** can be expressed as

$$n = \left(0, \quad 0, \quad 1\right) \tag{S5}$$

Therefore, in the presence of the external electric-field, the heliconical superstructure appears between helicoidal superstructure and the unwound state with corresponding thresholds of $E_1$ and $E_2$, which can be calculated using

$$E_2 = \frac{2\pi}{P_0}\frac{K_2}{\sqrt{\Delta\varepsilon\varepsilon_0 K_3}} \tag{S6}$$

$$E_1 \approx E_2 \frac{\eta\left[2+\sqrt{2(1-\eta)}\right]}{1+\eta} \tag{S7}$$

Where $\eta = K_3/K_2$, denotes the ratio of the bend and the twist elastic constants. The last equation is an approximation in the case of a small $\eta$.

# S2. Performance of the helical superstructure transformation with electrical stimulus

The heliconical state in CLC demonstrate here is different from the similar arrangement of LC director in chiral smectic C phase (*17*) and twist-bend nematic phase (*19*). Electric-field applied along the helical axis can rearrange the LC director along itself and thus reduce the heliconical pitch $P$ and oblique angle $\theta$ without deforming the helical axis. This characteristic endows the heliconical superstructure with peculiar tunable performance. The heliconical pitch $P$ is inversely proportional to the electric-field following as

$$P = \frac{2\pi}{E}\sqrt{\frac{K_3}{\varepsilon_0 \Delta\varepsilon}} \tag{S8}$$

And the equation for oblique angle $\theta$ as a function of the electric-field can be expressed as

$$\sin^2\theta = \frac{\eta}{1-\eta}\left(\frac{E_2}{E}-1\right) \tag{S9}$$

Then we employ numerical simulations to estimate the electric-field tunable pitch length $P$ and oblique angle $\theta$ and how important is the value of $\eta$ for the tunable range. As shown in fig. S2A, we have obtained the evolution of pitch length $P$ and oblique angle $\theta$ in the helicoidal, heliconical and unwound states with the gradual increase of the electric-field. $P_0$ is the pitch of the initial helicoidal superstructure which is determined by the chiral dopants. And the $\eta$ value of CLC system is varied between 0.084 and 0.491. Taking $\eta$=0.084 as an example, when the electric-field is below threshold value $E_1$, the CLC material could self-assemble into the helicoidal state and the corresponding pitch length and oblique angle almost remain constant when the electric-field increases (*i.e.*, $P/P_0 \approx 1$, $\theta \approx 90°$). As long as the electric-field exceeds the threshold value $E_1$, the CLC material transforms into the heliconical state. The oblique angle jumps to around 30° and then gradually decreases to near 0° while the pitch length shows the same trend. Finally, the CLC material is completely unwounded by the electric-field and the corresponding oblique angle and pitch length become 0 and infinite, respectively. It is noteworthy that the tuning range of the oblique angle $\theta$ and the relative pitch length $P/P_0$ of the heliconical superstructure depends solely on the parameter $\eta$, irrespectively of other parameters. The smaller the value of $\eta$, the wider the electric-field tunable range of the heliconical structure becomes. Experimentally measured dependence of the reflection wavelength of the heliconical

superstructure on the electric-field at different $\eta$ values is shown in fig. S2, which further demonstrates the influence of the parameter $\eta$ on the tuning range of the heliconical superstructure.

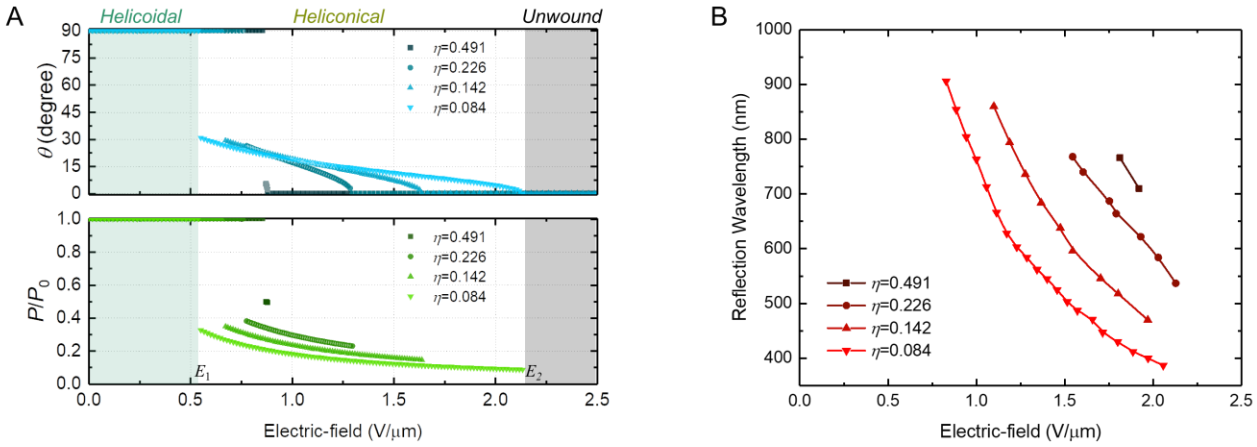


**Fig. S2. Electrical tuning performance of the heliconical superstructure.** (**A**) Dependence of the oblique angle and the pitch length on the applied electric-field. The material parameter $\eta$ is varied between 0.084 and 0.491. The oblique angle (or the relative pitch length) implies the transformation among different superstructures, *i.e.*, when the oblique angle is around 90° (with the relative pitch length being around 1), it corresponds to the helicoidal superstructure; when the oblique angle is between 0° and 90° (with the relative pitch length being between 0 and 1), it corresponds to the heliconical superstructure; when the oblique angle is 0° (with the relative pitch length being infinite), it corresponds to the unwinding state. (**B**) The experimentally measured reflection wavelength of the heliconical superstructure as a function of the electric-field at different $\eta$ values.

Such delicate field-dependent pitch and oblique angle tunability gives the heliconical superstructure a wide range of the periodicity and the effective refractive index modulation in the spiral direction, thereby achieving a selective control over the reflection band or the photonic band gap. To further confirm the optical properties of the heliconical superstructure, we utilize the Berreman's 4×4 matrix method (*23*,*35*) (the detailed description is in the section 4) to numerically analyze the selective reflection properties including the circular polarization selectivity, the reflective intensity, and the reflection band under different electric-fields. Calculation parameters are listed below: initial pitch $P_0$=2.60 μm at the photostationary state

with right-handedness helix, birefringence $n_e$=1.555, $n_o$=1.721, dielectric anisotropy $\varepsilon_{//}$=11.9, $\varepsilon_{\perp}$=5.9, which have been measured in our material system. $\eta$ value of the CLC material is 0.083 which is deduced to by theoretical fitting the experimental data (Fig. 2B). The reflection spectra in the case of normal incidence are shown in fig. S3. Only when the circular polarization of the incident light and the heliconical structure having the same handedness, can we obtain distinct reflection band, *i.e.*, a selectivity of the Bragg reflection band to the circular polarization. So, left-handedness circular polarized light (*L-CP*) will pass through the helical structure without reflection. The interference fringes in the background in fig. S3 are due to the finite thickness of the CLC material. For incidence with right-handedness circularly polarized light (*R-CP*), during the enhancement of electric-field, the calculated reflection band exhibits a blue-shift, accompanied by a decrease in the reflection half-width and reflection intensity which agrees well with experimental results (Fig. 2B). The reason for blue-shift of the reflection wavelength is due to the decreasing of pitch length. While the reflectance and the full width at half maximum of the reflection band are decreased because the oblique angle is getting smaller.

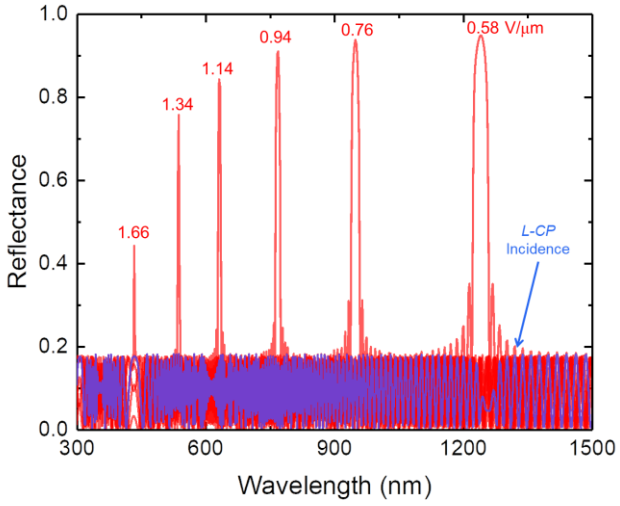


**Fig. S3. Simulated selective reflection spectra in the right-handed heliconical superstructure with various applied electric fields in the cases of R-CP incidence and L-CP incidence.**

## S3. Performance of the helical superstructure transformation with electric-field and light stimuli

To further understand the photo-tuning dynamics of the heliconical superstructure under electric and optical stimuli in Fig. 2C, in this part, we would discuss the influence of the chirality of the CLC system on the switching performance of the heliconical superstructure. Where chirality is defined as

$$q_0 = \pm\frac{2\pi}{P_0} = 2\pi \cdot C \cdot HTP \tag{S10}$$

denoting the chiral strength determined by intermolecular interactions. Where $C$ is the concentration of chiral dopant and $HTP$ is the helical twisted power of chiral dopant. The positive value indicates a right-handedness of the LC helix, while the negative value indicates a left-handedness of the LC helix. For our photo-responsive chiral dopant, the value of $HTP$ is related to the light stimulus. Thus, we can indirectly explain the effect of light stimulus by assessing the impact of system chirality changes on overall performance.

As shown in fig S4, we have obtained the evolution of the transformation threshold value $E_1$ and $E_2$ with the gradual changes of the chirality $q_0$; pitch length $P$ and oblique angle $\theta$ in the helicoidal, heliconical and unwound states with the gradual changes of the chirality $q_0$ under several specific electric-field value. When chirality decreases, the threshold value $E_1$ and $E_2$ both decreases, which is attributed to the requirement of a comparable elastic toque to complete with the twist toque (fig. S4A). Thus, fixed at a given electric-field $E$ and decreasing chirality $q_0$, we can estimate the switching performance under the combination of electric-field and light stimulations. Taking $E$=0.58V/μm as an example. When the chirality is large enough, CLC material exhibits helicoid state, with oblique angle $\theta$=90° (fig. S4B) and pitch length $P$ remain constant equal to $2\pi/q_0$ (fig. S4C). When chirality gradually decreases, helicoid state would like to transform into heliconical state accompanied by abrupt changes of pitch length $P$ and oblique angle $\theta$. However, oblique angle $\theta$ decreases when chirality decreases but pitch length $P$ keeps constant at heliconical state. When the chirality is weak enough, CLC material exhibits unwound state, with oblique angle $\theta$=0° and pitch length $P$ becoming infinite.

As a result, during the photo-tuning curves in Fig. 2C, when chirality is decreased by the photo-isomerization of the chiral switch, the intensity of the reflection gradually decreases along with a small amount of spectral blue shift (<10 nm). As chirality further decreases at a point when $E_2$ is below the applied field, it appears the dark state with zero reflection. Further light irradiation generating handedness inversion, the chirality increases and the heliconical superstructure re-forms with a gradually increased reflection intensity accompanied by a little spectral red shift (<10 nm). We further calculated the reflection spectra using the Berrman's 4 × 4 matrix method during the photo-tuning process in fig. S5, which further collaborate our experimental and theoretical results. Therefore, a couple of electric-field value and light dose can determine a helix state.

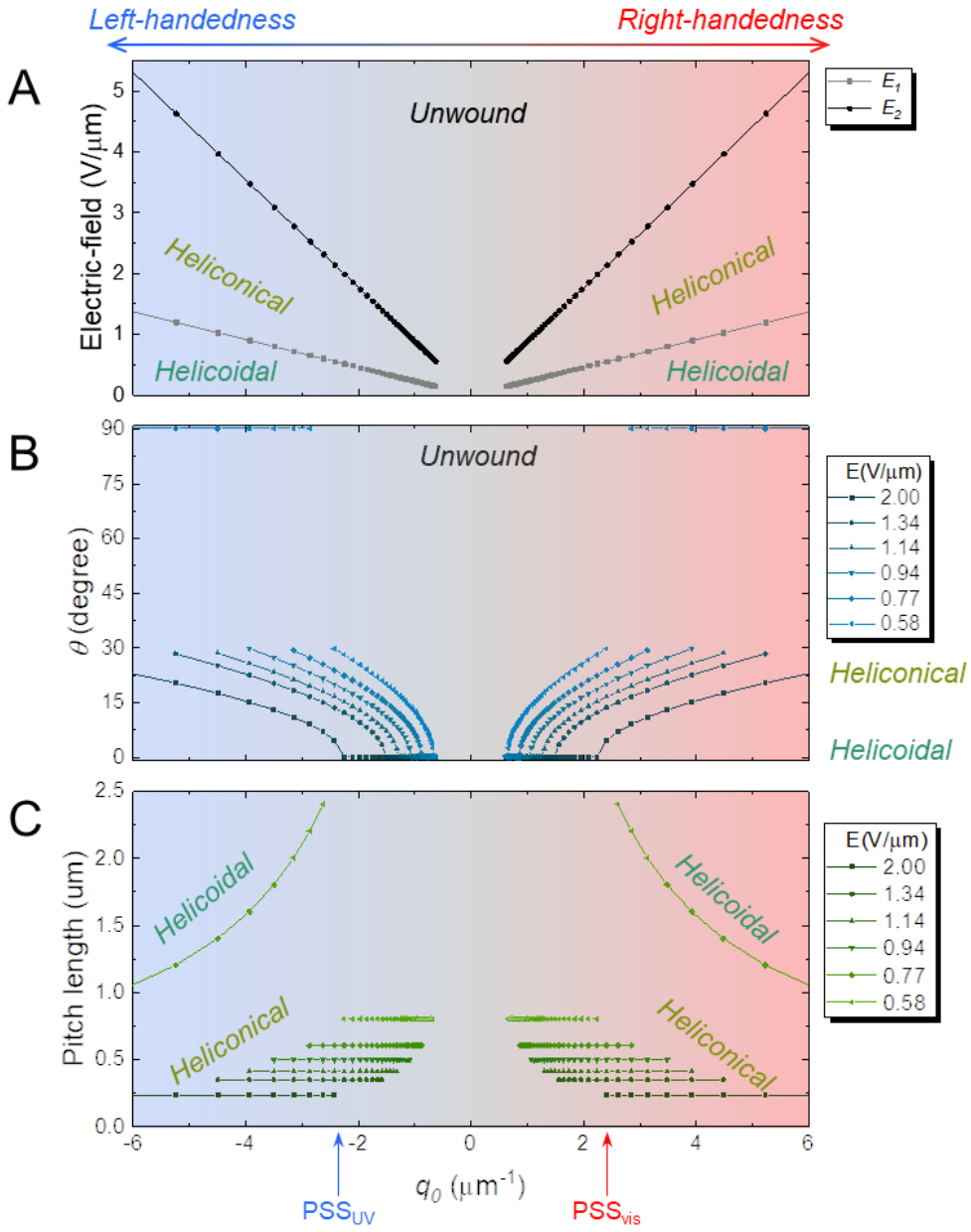


**Fig. S4. Theoretical investigation of the effects of the photoinduced chirality changes on switching performance.** (**A**) Dependence of the threshold electric-field $E_1$ and the unwinding electric-field $E_2$ on chirality. (**B**) Dependence of the oblique angle $\theta$ on chirality at different electric-fields. (**C**) Dependence of the pitch length $P$ on chirality at different electric-fields. The right- and left-part denotes the right-handedness and the left-handedness helical superstructure with positive and negative chirality $q_0$, respectively. The $\eta$ value is maintained as 0.084.

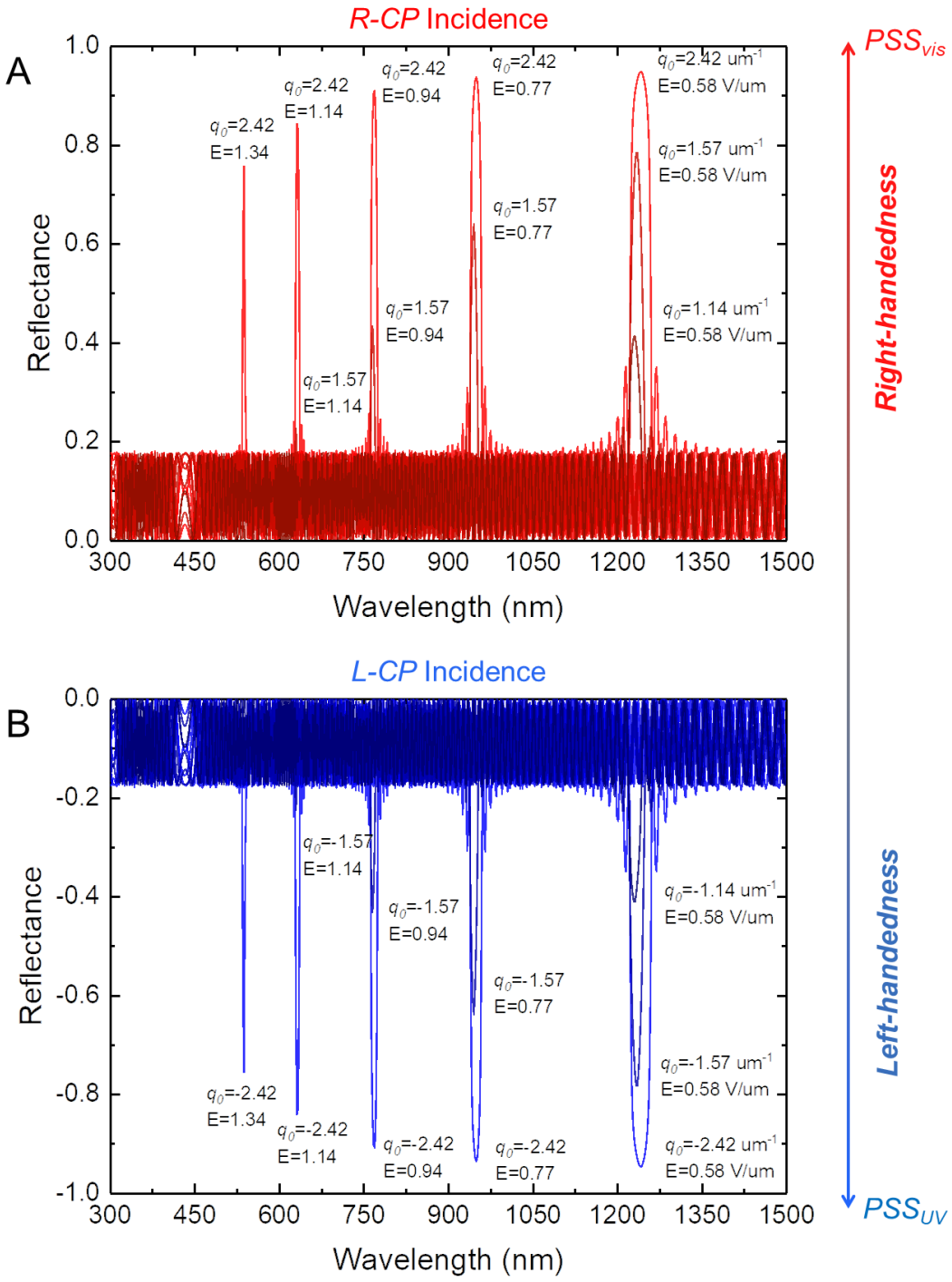


**Fig. S5. Calculated reflection spectra from the heliconical superstructure as a function of the electric field and light stimuli.** (**A**) For the right-handedness and (**B**) left-handedness heliconical superstructure, respectively. The chirality $q_0$ is varied between 1.14 $\mu m^{-1}$ and 2.42 $\mu m^{-1}$.

# S4. Berreman's 4 × 4 matrix method

In the section 2, we have calculated the refection spectra from the heliconical superstructure based on the Berreman's 4 × 4 matrix method. This theoretical approach could provide precise transmission and reflection coefficients when lights transmitting through the optical layers. The foundations of this approach and its compatibility with the helix superstructure could be explained in detail here. For a uniaxial CLC, when it is arranging in the oblique helicoid state with oblique angle $\theta$, the director is

$$\vec{n} = \begin{pmatrix} n_x \\ n_y \\ n_z \end{pmatrix}^T = \begin{pmatrix} \cos(\frac{2\pi}{P})\sin\theta \\ \sin(\frac{2\pi}{P})\sin\theta \\ \cos\theta \end{pmatrix}^T \tag{S11}$$

Then the dielectric tensor is

$$\vec{\vec{\varepsilon}} = \begin{pmatrix} \varepsilon_\perp + \Delta\varepsilon n_x^2 & \Delta\varepsilon n_x n_y & \Delta\varepsilon n_x n_z \\ \Delta\varepsilon n_x n_y & \varepsilon_\perp + \Delta\varepsilon n_y^2 & \Delta\varepsilon n_y n_z \\ \Delta\varepsilon n_x n_z & \Delta\varepsilon n_y n_z & \varepsilon_\perp + \Delta\varepsilon n_z^2 \end{pmatrix} \tag{S12}$$

Where $\varepsilon_\perp = n_o^2$ and $\Delta\varepsilon = \varepsilon_\parallel - \varepsilon_\perp = n_e^2 - n_o^2$. The Berreman matrix is given by

$$\vec{\vec{Q}} = \frac{1}{\left(\varepsilon_\perp + \Delta\varepsilon n_z^2\right)} \begin{pmatrix} 0 & \left(\varepsilon_\perp + \Delta\varepsilon n_z^2\right) & 0 & 0 \\ \varepsilon_\perp\left[\varepsilon_\perp + \Delta\varepsilon\left(n_x^2 + n_z^2\right)\right] & 0 & \varepsilon\ \Delta\varepsilon n_x n_y & 0 \\ 0 & 0 & 0 & \varepsilon_\perp + \Delta\varepsilon n_z^2 \\ \varepsilon_\perp \Delta\varepsilon n_x n_y & 0 & \varepsilon_\perp\left(\varepsilon_\perp + \Delta\varepsilon n_z^2\right) + \varepsilon_\perp \Delta\varepsilon n_y^2 & 0 \end{pmatrix} \tag{S13}$$

Outside the cholesteric film, we assume that the medium is an isotropic medium with the refractive index $n$=1. On top of the cholesteric film, there is incident light and reflected light, and the actual Berreman vector is the sum of the Berreman vectors of the incident light and reflected light. For the incident light, the Berreman vector is

$$\vec{\psi}_i = \begin{pmatrix} E_{xi} & E_{xi} & E_{yi} & E_{yi} \end{pmatrix}^T \tag{S14}$$

Where $E$ is the electric-field components of the transmitted and reflected light. For the reflected light, because it propagates in the reverse direction, the Berreman vector is

$$\vec{\psi}_r = \begin{pmatrix} E_{xr} & -E_{xr} & E_{yr} & -E_{yr} \end{pmatrix}^T \tag{S15}$$

At the bottom of the cholesteric film, there is only the transmitted light whose Berreman vector is

$$\vec{\psi}_r = \begin{pmatrix} E_{xr} & -E_{xr} & E_{yr} & -E_{yr} \end{pmatrix}^T \tag{S16}$$

We divide the cholesteric film into *N* slabs with thicknesses Δz. The Berreman vectors at the boundaries between the slabs are

$$\vec{\psi}(0) = \vec{\psi}_i + \vec{\psi}_r, \tag{S17}$$

$$\vec{\psi}(1) = \ddot{P}(z_1) \cdot \vec{\psi}(0) \tag{S18}$$

$$\vec{\psi}(2) = \ddot{P}(z_2) \cdot \vec{\psi}(1) = \ddot{P}(z_2)\ddot{P}(z_1) \cdot \vec{\psi}(0) \tag{S19}$$

…….

$$\vec{\psi}_t = \vec{\psi}(N) = \prod_{i=1}^{N} \ddot{P}(z_i) \cdot \vec{\psi}(0) = \prod_{i=1}^{N} \ddot{P}(z_i) \cdot (\vec{\psi}_i + \vec{\psi}_r) \tag{S20}$$

where the $\ddot{P}$ for each slab can be numerically calculated by fast Berreman method (*36*). Solving the above Equations, the outgoing transmitted light $\vec{\psi}_t$ and outgoing reflected light $\ddot{\psi}_r$ can be found. Finally, the reflection intensity corresponding to each wavelength in the spectrum can be obtained by

$$T = \left(E_{xt}^2 + E_{yt}^2\right) / \left(E_{xi}^2 + E_{yi}^2\right) \tag{S21}$$

$$R = \left(E_{xr}^2 + E_{yr}^2\right) / \left(E_{xi}^2 + E_{yi}^2\right) \tag{S22}$$

# S5. Optimization of the cholesteric liquid crystal material system

According to the above investigations, the CLC material parameter $\eta$ plays a critical role in determining the switching performance among different helix configurations. In order to obtain a stable heliconical superstructure with a wide pitch tuning range, it is important to minimize the $\eta$ value, which means the bend elastic constant $K_3$ should be sufficiently small. So, we have chosen a peculiar LC dimer that yields the necessary smallness of $K_3$ as the main components for our CLC mixture. The chemical structure of the achiral LC dimer 1'',7''-bis(4-cyanobipheny1-4'-yl)heptane($NC(C_6H_4)_2(CH_2)_7(C_6H_4)_2CN$ named CB7CB is shown below, which is composed of two rod-like cyanobiphenyl moieties directly linked by a flexible alkyl chain. CB7CB shows a nematic phase in the temperatrure range of 103 $^oC$ to 116 $^oC$ between the isotropic and twist-bend nematic ($N_{tb}$) phase (*37,38*). While in its $N_{tb}$ phase (84.5 $^oC$ – 103 $^oC$), CB7CB molecules self-organize to form a heliconical superstructure with a nanoscale period about 10 nm existing as a ground state in the absence of any external fields and any chiral dopants. Besides, such nanoscale heliconical superstructure should break into left-handedness and right-handedness domains due to the achiral chemical structure which distinguishes itself from the above heliconical superstructure.

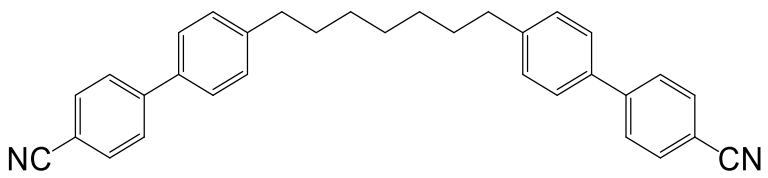


**Fig. S6. Chemical structure of the LC dimer CB7CB.**

When the CLC material is composed of the pure LC dimer CB7CB and appropriate chiral dopants, it exhibits cholesteric phase with a temperature range between 100 $^oC$ and 113 $^oC$, presenting difficulties for practical devices. In order to facilitate the material working in the room temperature and expand the temperature range of cholesteric phase, we have tried to mix the nematic LC E7 with the CB7CB to forming the host of CLC. In order to optimize the composition of the host LC, we have experimentally tested the temperature range of cholesteric phase as a function of the material composition and the experimental data are presented in fig. S7A. The temperature range of cholesteric phase increases as the composition ratio

of E7 increases in the host. The CLC working temperature range covers the room temperature when the concentration ratio, E7:CB7CB, in the host reaches 55:45. As the concentration ratio further increases, the temperature range of cholesteric phase continues to increase, however the electric-field induced heliconical state is disappeared due to the decoupling of the bend and twist effects in the system. Furthermore, it is noteworthy that the tuning performance of the heliconical superstructure from the optimized CLC material is temperature dependent. As shown in fig. S7B, the tuning range of the reflection wavelength narrows as the temperature increases, which is likely due to the increase of $K_3$ and $\eta$ value (*39*). However, the tuning properties deteriorate when the temperature approaches the phase transition temperature (cholesteric phase to $N_{tb}$ phase). Besides, the whole tuning process for the electric-field controllable reflection band is reversible and repeatable as long as the experimental conditions are invariable. Hence, such CLC material have been optimized to work at room temperature of 25 $^{o}$C. It is noteworthy that the forward and backward tuning curves are nearly overlapped, which indicates the whole transformation process is almost hysteresis-free. The multi-state reversible helical superstructure switching depends on sophisticated matching of experimental and material parameters such as the temperature, the strength of electric-field, and the bend and twist elastic constants.

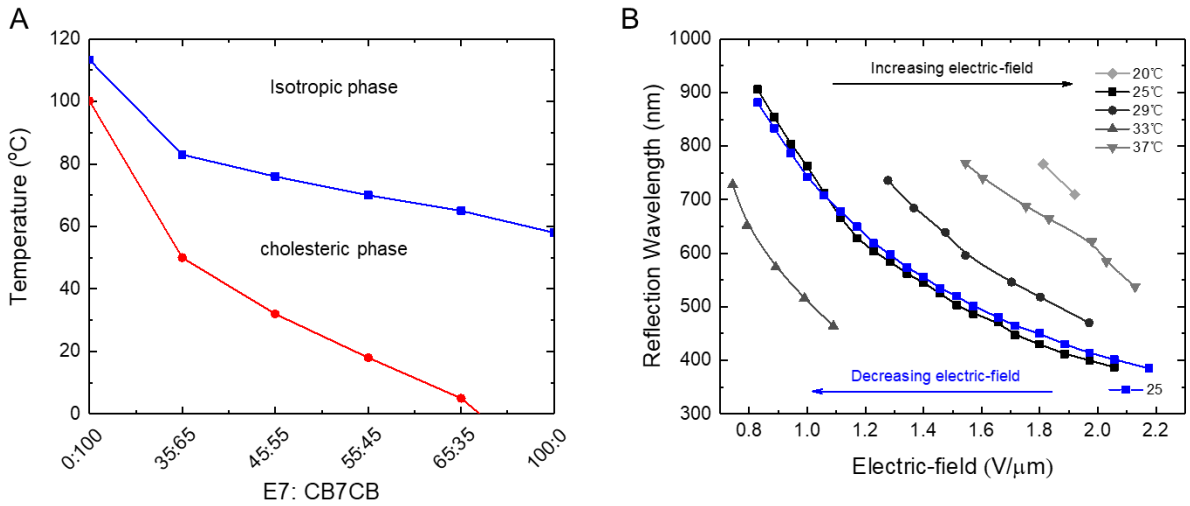


**Fig. S7. Optimization of the cholesteric LC material system.** (**A**) Phase sequence of the CLC material as the change of the composition of the host of the CLC (content of chiral dopant, R811: 0.5 wt%, (*s*,*s*)-BTTC: 3.0 wt%). (**B**) Effects of temperature on electrical tuning performance of the heliconical superstructure. The dependence of the reflection wavelength

on the electric-field at different temperatures was experimentally measured for the CLC material. The concentration ratio between E7 and CB7CB in the host is 55:45.

The dithienylcyclopentene-based photo-responsive chiral molecular switch shows excellent thermal stability and fatigue resistance due to the extreme high activation energy of ring-opening reaction. The ring-open isomer in the $PSS_{vis}$ state is at the energy minimum and is thermodynamically stable. The UV light irradiation induces the photoisomerization reaction which results in the ring-closed isomer. The ring-closed isomer has a higher energy level and is apt to thermal relax into the open-ring isomer even no visible light is present. However, the thermal relaxation could be heavily slowed down by a sophisticated chemical engineering of the molecular structure to increase the activation energy in opening the ring. The real-time visible light absorption in tetrahydrofuran (THF) solution at 550 nm of the ring-closed isomer was used to monitor the thermal relaxation process in 25 $^{o}$C (fig. S8B), and it shows no obvious degradation even after 10 hours. We have further provided the cyclical operation behaviors of the photo-responsive chiral switch under alternate UV and visible light irradiation (fig. S8C). After a number of operation cycles, the visible absorption of the ring-closed isomer shows barely no attenuation, indicating good stability.

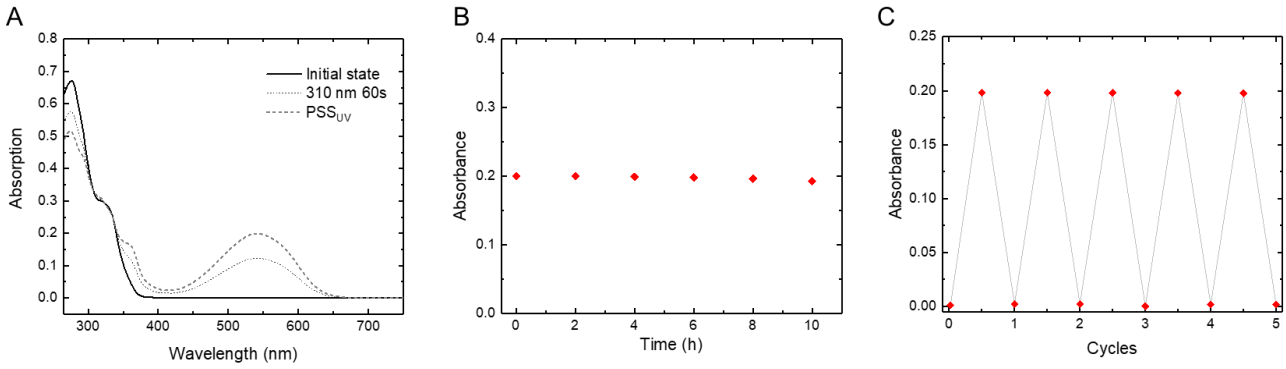


**Fig. S8. UV-visible changes of (*s*,*s*)-BTTC in tetrahydrofuran solution and the thermal stability and fatigue resistance of closed-ring isomers.** Thermal stability of closed-ring isomers in THF is monitored by the absorbance at 550 nm. Cyclical absorbance of (*s*,*s*)-BTTC in THF at 550 nm as the solution was repeatedly irradiated with UV light (310 nm) and visible light (530 nm).

In order to achieving a noncontact light modulation on both helical pitch length and the handedness, the photo-responsive chiral molecular switch (*s*,*s*)-BTTC was mixed into the system. Its doping concentration determines the initial pitch length of the corresponding helicoidal superstructure and the dynamic spectral range of the reflection band stimulated by electric-field. As discussed in part 3 of the Supplemental Information, the threshold electric-field to induce the heliconical superstructure has a linear dependence on the initial pitch length of helicoidal structure. Besides, the increase of (*s*,*s*)-BTTC would enhance the photo-responsiveness of the system.

In addition, a small amount of photo-inactive chiral dopant R811 was introduced to balance the difference on HTP of the open form and closed form (*s*,*s*)-BTTC, thereby enabling the similar dynamic reflection spectral ranges of right-handed and left-handed heliconical system under the stimulation. With a delicate optimization of the components, we finally achieve a dynamic and reversible transformation of a soft helical superstructure among the helicoidal, heliconical and their inverse helices, together with a tunability on the helical pitch, by the combination of electric-field and light stimulations.

# S6. Verification of polarization state

To verify the circular polarization state of the reflected light and emission light, a quarter wave plate (QWP) and a polarizer are employed to implement polarization transformation. The evolution process can be calculated by Jones matrix method (*35*). Jones matrix for circularly polarized light is described by

$$E = \frac{1}{\sqrt{2}}\begin{pmatrix} 1 \\ \pm i \end{pmatrix} \tag{S23}$$

Where the positive and negative signs in the formula represent right- and left-handed polarized light, respectively. Jones matrix for a QWP with its slow axis parallel to the *x* axis

$$M_{QWP} = \begin{pmatrix} 1 & 0 \\ 0 & i \end{pmatrix} \tag{S24}$$

So, if the incident light with right-handed circularly polarization passes through the QWP, the polarization of the outgoing light is

$$E_{\mathrm{o}} = M_{QWP} * E_i = \begin{pmatrix} 1 & 0 \\ 0 & i \end{pmatrix}\begin{pmatrix} 1 \\ i \end{pmatrix} = \frac{1}{\sqrt{2}}\begin{pmatrix} 1 \\ -1 \end{pmatrix} \tag{S25}$$

Then the outgoing light converts to linearly polarized light with its polarization direction making an angle of -45° to the *x* axis. If the incident light with left-handed circularly polarization passes through the QWP, the polarization of the outgoing light is

$$E_{\mathrm{o}} = M_{QWP} * E_i = \begin{pmatrix} 1 & 0 \\ 0 & i \end{pmatrix}\begin{pmatrix} 1 \\ -i \end{pmatrix} = \frac{1}{\sqrt{2}}\begin{pmatrix} 1 \\ 1 \end{pmatrix} \tag{S26}$$

Then the outgoing light converts to linearly polarized light with its polarization direction making an angle of 45° to the *x* axis. Further passing through an analyzer with its transmission axis at 45°, the outgoing light will be ideally eliminated.

# S7. Laser performance

We have characterized the optical properties of the laser dye DCJ which is utilized in this work as the gain medium for the induction of laser emission from the tunable heliconical superstructure. The chemical structure of DCJ is given in the upper left of fig. S9. DCJ is a novel small molecule laser dye with a molecular weight of 453.6 which is beneficial for the homogeneous doping in the LC host. Its absorption spectrum is measured using a UV-visible spectrophotometer (Analytik Jena, Specord Plus) and is given as the green curve in fig. S9. The absorption spectrum peaks around 520 nm and a decent absorption efficiency is guaranteed at the pumping wavelength of 532 nm. The fluorescence spectrum is measured using a fluorescence spectrometer (Shimadzu, RF-6000) where a continues laser at the wavelength of 532 nm is using for pumping. The fluorensence spectrum is shown as the red curve in fig. S9 where its fluorescence spectrum covers a borad wavelength range from 575 nm to 740 nm and peaks aournd 630 nm, indicating a wide gain spectrum for the tunable lasing investigation in this work. The doped LC mixture is utilized as the tesing samples to avoid the effects of the host on the optical peoperties of the laser dye.

Figure S10 depicts the dependence of the emission intensity on pump energy for the heliconical resonators with different handedness. When the pump energy is below the laser threshold, which means the optical loss in each rounded loop could not be compensated by the optical gain through stimulated emission. The output emission from the superstructure is thus dominated by omnidirectional fluorescence, characterized by a broad band spectrum and a low emission intensity. As the pump energy increases, the optical gain exceeds the cavity loss, and the stimulated emission takes the role. As photons generated by stimulated emission have same properties in terms of the wavelength, the polarization and the propagating direction, the collected emission shows a narrow bandwidth with an abrupt increase in emission intensity. As a result, the laser threshold could be determined by the intersection of the two linear curves fitted to the two regimes. The experimental data and the fitting curves are shown in fig. S10. The right-handed heliconical cavity shows a threshold of 1.73 uJ/Pulse while the left-handed one shows a threshold of 1.80 uJ/Pulse, demonstrating the effectiveness and reliability of the heliconical superstructure as the laser resonator.

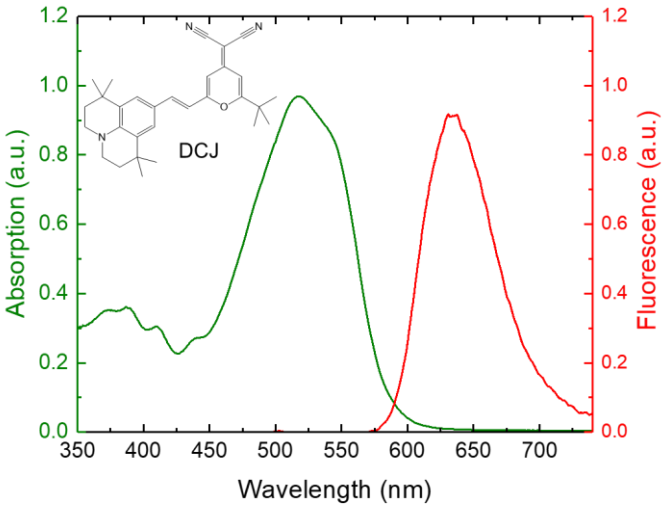


**Fig. S9. Characterization of the optical properties of the laser dye DCJ.** The chemical structure of the laser dye DCJ is given in the upper left. Its absorption spectrum and the fluorescence spectrum are shown in the green and red curves, respectively.

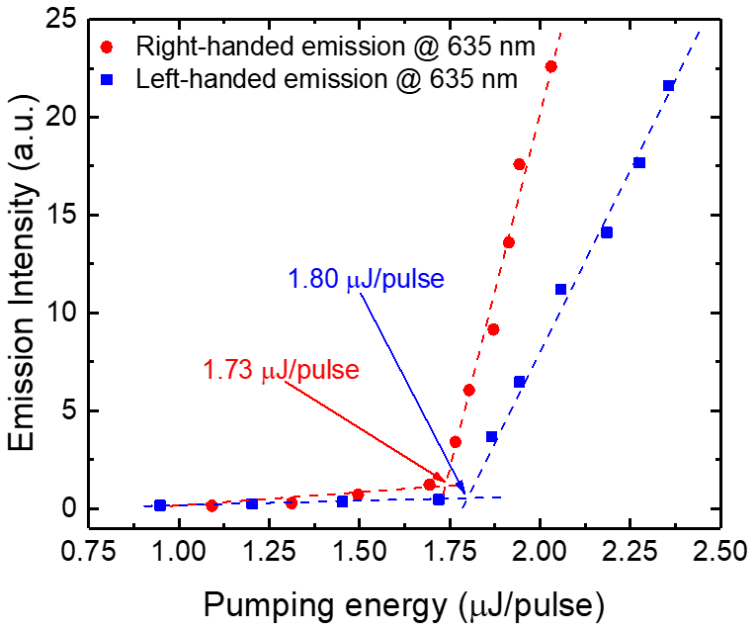


**Fig. S10. Emission intensity as a function of pump energy for the right-handed heliconical resonator and the left-handed heliconical resonator.**

# S8. Optical diffraction from the micro-patterns

The mirco-patterned superstructures in Fig. 4 formed by the different chiral properties exhibit interesting optical diffractions which is owing to the periodic distribution of effective refractive index. In the dark regions, LC molecules arrange in homeotropic alignment with the effective refractive index $n_1=n_o$ along $z$ axis. While for chiral regions, the effective refractive index of heliconical superstructure can be written as

$$n_2 = \sqrt{(2n_o^2 + n_{e,eff}^2)/3} \tag{S27}$$

$$n_{e,eff} = \frac{n_e n_o}{\sqrt{n_e^2 \cos^2\theta + n_o^2 \sin^2\theta}} \tag{S28}$$

Where $n_o$ and $n_e$ denote the ordinary refraction index and extraordinary refraction index of LC, respectively. Diffractive properties of the sample with light patterned superstructures are characterized experimentally. The probe laser (He-Ne laser, 633 nm), after being expanded and collimated is normally impinged to the sample. Then the diffractive light can be received in the black screen.